The effect of laser scanning speed on microstructural evolution during direct laser deposition 12CrNi2 alloy steel

Yue Zhou[a], Suiyuan Chen[a,*], Xueting Chen[a], Jing Liang[a], Changsheng Liu[a], Mei Wang[b]

[a] Key Laboratory for Anisotropy and Texture of Materials, Ministry of Education, Key Laboratory for Laser Application Technology and Equipment of Liaoning Province, School of Materials and Engineering, Northeastern University, 110819, China
[b] Shenyang Dalu Laser Technology Co. Ltd., China

HIGHLIGHTS

- The microstructural evolution of DLD 12CrNi2 with laser scanning speed was studied.
- The relationship between laser scanning speed and microstructure were fitted.
- Bainite ferrite with a width of 500–600 nm was observed due to high energy input.
- The impact toughness could reach 80 J/cm^2 due to a large amount of ferrite phase.

ARTICLE INFO

ABSTRACT

This paper focused on the effect of different laser scanning speed (4 mm/s, 5 mm/s, 6 mm/s and 7 mm/s) on the microstructural evolution of direct laser deposition (DLD) 12CrNi2 alloy steel, and analyzed the relationship between microstructure and performance of DLD-processed samples. The results showed that the microstructure in the middle of as-deposited samples consisted of a large amount of bainite, a small amount of martensite (M) and ferrite (F). With the increase of laser scanning speed, the fraction of ferrite decreased from 55.6% to 14.7%, while that of martensite increased from nearly 0% to 4.9%. Besides, as increasing the laser scanning speed, granular bainite (GB) transformed into lath bainite (LB) due to the increase of cooling rate, and the fraction of LB reached the maximum of 29.9% when the scanning speed was 7 mm/s. In addition, the functions about the relationship between laser scanning speed and phase fractions were fitted in order to provide a theoretical basis for the design of DLD process parameters. EBSD maps of as-deposited samples exhibited anisotropy due to the complex heat flux direction during the multi-layer laser deposition process. With the increase of laser scanning speed, the grain size showed a downward trend from 5.89 μm^2 to 3.44 μm^2. The sample fabricated at 7 mm/s contained more LB and M, leading to the highest mean microhardness of 355 ± 6 HV$_{0.2}$. The sample fabricated at 6 mm/s exhibited the best wear resistance due to its optimum combination of hardness and toughness. Because of a large amount of ferrite with optimal toughness, the sample fabricated at 4 mm/s had the best impact toughness of a_{ku} = 80 J/cm^2.

1. Introduction

Additive Manufacturing (AM), a subtractive manufacturing technology, is capable of fabricating metal parts rapidly with the aid of computer technology. Compared to conventional methods, it can produce complex shaped products at reduced processing time and costs [1–3]. Direct Laser Deposition (DLD) is a type of additive manufacturing (AM) process, which consists of powder feeding and in-situ laser melting [4].

Alloy steel is a widely used metal material, and recent years, DLD alloy steel has been adopted in automobile, nuclear power station, aero industry as a manufacturing method as well as a repair method of key parts [5–8]. DLD alloy steel is a non-equilibrium metallurgical process, the high cooling rate during DLD process usually results in complicated phase structures, which consequently affect the comprehensive performance of DLD-processed samples [9], so the study on microstructure evolution with the variation of process parameters during DLD alloy steel process is necessary. In recent years, there have been many studies

---

focusing on how laser process parameters to affect the formability and microstructure of the as-deposited samples. Casalino [10] et al. explored the microstructure, the mechanical and surface properties and the statistical optimization of selective laser melting (SLM) maraging steel. They found process parameters could influence the density of parts, and the mechanical and surface properties correlated positively to the density of samples. The result demonstrated that the laser power greater than 90 W and the scanning speed less than 220 mm/s was the optimal process parameter. Wang [11] et al. studied the effect of laser mode (pulse or continuous wave laser) and pulse laser parameters (T-pulse and T-pause) on the microstructure, hardness, residual stress and tensile properties of the laser deposition AISI316L stainless steel thin-walled parts. Kurzynowski [12] et al. evaluated the impact of laser power and scanning strategies on microstructure, texture and tensile properties of the SLM-processed 316L stainless steel samples. The results showed that the samples fabricated at different laser power and scanning strategy had different cellular substructure of austenite, the amount of ferrite and texture. Compared to hot-rolled SS316L sheet, there was a double increase of yield strength accompanied by a 1.4 times reduction of elongation of as-deposited tensile samples. Mazumder et al. [13] investigated the effects of different laser process parameters on the geometry and material properties of direct metal deposition (DMD) Inconel 718 superalloy, and used linear regression method to construct the models between different parameters and the dimensional characteristics. Besides, the relationship between cooling rate and different parameters was also analyzed. The results showed that laser power and laser scanning speed were the two most significant factors affecting the size and microstructure of the as-deposited layer. Zhang et al. [14] studied the microstructure, phase characteristics and mechanical properties of laser metal deposition (LMD) 316 stainless steel. It found that the microstructure of LMD 316 stainless steel consisted of elongated dendrites grown from the matrix and had good mechanical properties. In addition, different laser process parameters had different effects on the microstructure and mechanical properties of the as-deposited samples. Among them, the scanning speed had the most significant effect on the microstructure, mechanical properties and geometry of the as-deposited parts.

In our previous research [15], the effect of laser power on the evolution of bainite during DLD 12CrNi2 alloy steel process However, according to other studies [13,14], it is known that laser scanning speed had a greater impact on the microstructure of as-deposited samples, but rare papers researched the relationship between laser scanning speed and phase content. Different from our previous research, in this study, the effect of laser scanning speed on microstructural evolution (not only bainite phase) during DLD 12CrNi2 alloy steel process was investigated. More importantly, the functions about the relationship between laser scanning speed and phase fractions was fitted in order to provide a research method to the design of process parameters of DLD alloy steel.

2. Experimental procedure

As-received Q235 steel plate with the dimension of 100 mm × 100 mm × 10 mm was used as the substrate material, with the nominal composition in wt.%: C ≤ 0.22, Mn ≤ 1.40, Si ≤ 0.35, S ≤ 0.050, P ≤ 0.045 and balance Fe. 12CrNi2 alloy steel powder prepared by vacuum atomization was used as DLD initial material. The chemical composition of alloy steel powders material was (in wt.%): 0.144C, 0.745 Cr, 1.85 Ni, 0.278Si, 0.605 Mn, 1.7 Y, with balance Fe. Before the DLD process, the powders were dried for about 6 h at 80 ℃ in a vacuum drying oven. The morphology of 12CrNi2 alloy steel powder is shown in Fig. 1(a), and (b) exhibited powder size distribution.

As shown in Fig. 2, the DLD-processed 12CrNi2 alloy steel samples were fabricated efficiently by FL-DLS21 laser forming system with a maximum output power of 3000 W. The process parameters utilized in this study are provided in Table 1.

The porosity of DLD-processed 12CrNi2 alloy steel was measured by

X-ray CT system (Versa XRM-500) with the voxel size of 1.4 μm³. The sample was rotated 360° in order to acquire 1600 images, and the exposure time of each image was 6 s.

The phase composition was identified by X-ray diffraction at a scanning rate of 3°/min ranging from 20° to 120° with Cu Kα. In order to observe the metallography, the as-deposited samples were cut, polished and etched with a solution of 4 ml nitric acid and 96 ml ethanol for 10–15 s. Microstructural characterization and crystallographic orientation were achieved by optical microscopy (OM, OLYMPUS-GX71) and field emission scanning electron microscopy (FE-SEM, Shimadzu-SSX-550) equipped with an electron backscattered diffraction (EBSD) system. Chemical composition analysis of the DLD 12CrNi2 alloy steel was conducted by an energy dispersive spectrometer (EDS). In addition, fine phase structures were studied by high resolution transmission electron microscopy (HR-TEM, JEM-2100) at the voltage of 200 kV.

The microhardness of the cross section from surface to substrate was measured by MicroMet-5101 microhardness tester with a load of 2 N and a load-dwell time of 10 s. Dry sliding wear tests were carried out by multi-functional tester for material surface (MFT-4000), and the selected wear testing parameters were listed in Table 2. After dry sliding wear tests, the worn surfaces were rinsed with ethanol and dried with electric dryer, and the morphology of the worn surfaces were characterized by FE-SEM. The roughness and 3D surface of worn tracks were characterized by OL3000 confocal laser scanning microscopy (CLSM). The impact properties of Charpy U-notch samples were tested using a screen display impact tester (JBW-500). The dimensions of impact samples (according to ISO 148-1 standard) were shown in Fig. 3. The impact fracture surfaces of the broken samples were observed by FE-SEM.

3. Results and discussion

3.1. Porosity

Cracks, pores, inclusions are the main defects of laser additive manufacturing metal parts, which have a great influence on the formability and performance of the as-deposited samples [16]. Yadollahi et al. [17] studied that X-ray computed tomography (X-ray CT) could more accurately detect the distribution of voids inside as-deposited samples than the Archimede's drainage method. Fig. 4 visually shows the three-dimensional distribution of defects in DLD-processed 12CrNi2 alloy steel sample fabricated at different laser scanning speed. It can be seen that the distribution of defects was dispersed, and the main defect of DLD-processed 12CrNi2 alloy steel sample was pore. DLD was a rapid heat-up and cool-down process, and thus sometimes the gas did not escape in time, forming pores. In addition, Debroy et al. [3] found the use of alloy steel powder prepared by gas atomization for additive manufacturing often resulted in pores.

As shown in Fig. 5, different types of defects had different contrasts, the contrast of pore was greater than that of inclusion. Fig. 5 (a) was the cross-section morphology of the inclusion with an internal pore, and Fig. 5(b) presents the cross-section morphology of pores. Compared to the inclusion, the surface of pores was smoother and had a regular spherical shape. The data analysis results by Avizσ software are shown in Table 3, The porosity of DLD-processed alloy steel samples was calculated based on Eq. (1), as follows:

$$\text{Porosity} = \frac{\text{Total detected defect volume}}{\text{Total scanned volume}} \tag{1}$$

The porosity of four as-deposited samples was 0.075%, 0.018%, 0.026% and 0.074%, respectively, and it can be seen that the porosity of sample 2 was the lowest.

From Table 3, sample 1 and sample 4 had higher porosity than other samples due to inappropriate process parameters. When other process parameters were the same, low laser scanning speed (4 mm/s) could lead to a high energy input, which caused a disturbance on the surface
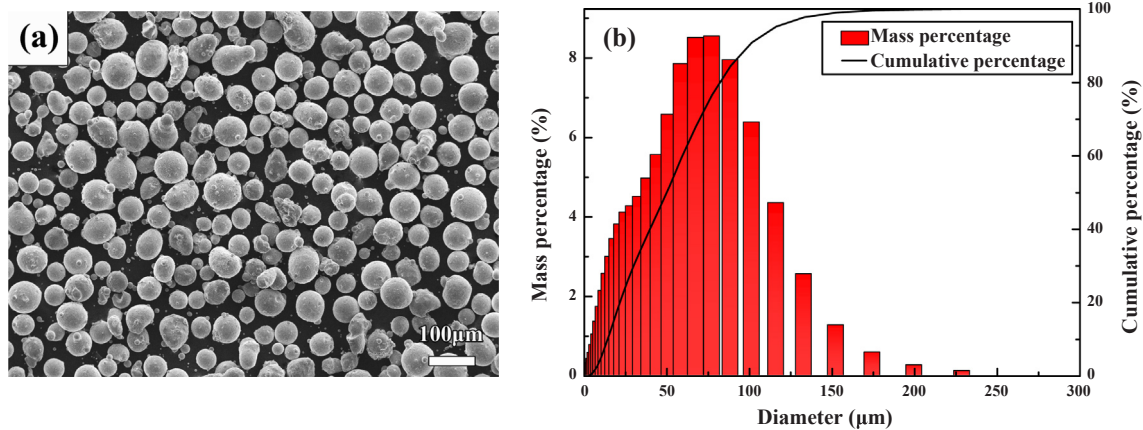
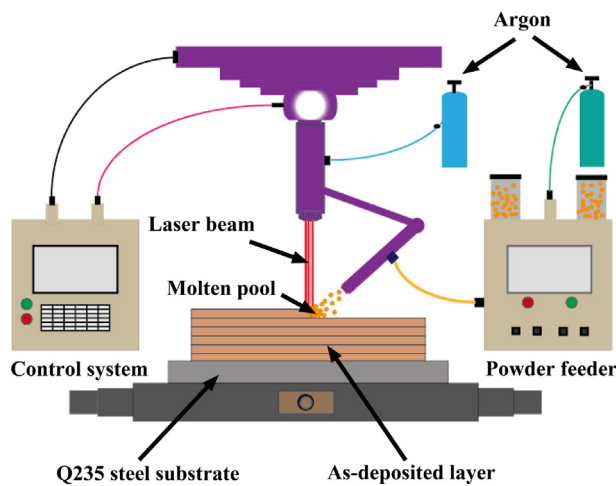**Fig. 1.** (a) 12CrNi2 powder morphology, (b) powder size distribution plot.

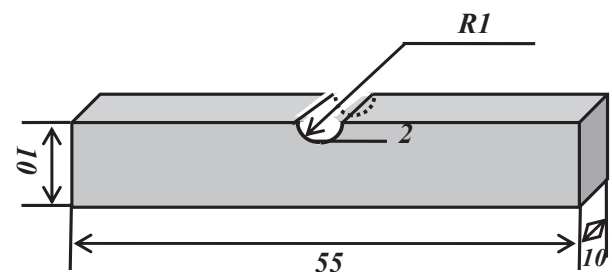**Fig. 2.** Schematic illustration of the DLD 12CrNi2 alloy steel process.

Fig. 3. Dimensions (in mm) of the Charpy U-notch impact sample.

formation and expansion.

3.2. Phase composition

As shown in Fig. 6(a), according to the equilibrium phase diagram of 12CrNi2 alloy steel simulated by JMATPRO dynamic simulation software, the equilibrium microstructure of 12CrNi2 alloy steel at the room temperature consisted of ferrite and pearlite. However, DLD 12CrNi2 alloy steel was a non-equilibrium metallurgical process with high heating and cooling rates, and thus the phase composition of DLD-processed sample was quite different from that of the sample produced by the equilibrium process. Besides, DLD was a multi-track and multi-layer process, the latter track or layer had a tempering effect on the processed part, and therefore the microstructure of as-doposited sample was complicated, and based on the simulated non-equilibrium phase diagram of 12CrNi2 alloy steel in Fig. 6(b), it can be speculated that the main phase of as-deposited sample was bainite. Microstructure is closely related to cooling rate in laser additive manufacturing, which is mainly affected by processing parameters such as scanning speed and laser power. It is difficult to obtain cooling rate experimentally due to the inherent property of its rapid solidification. Studies by Shao [21] and Zuo [22] have shown that scanning speed can directly affect the cooling rate, resulting in changes in microstructure and grain size during laser additive manufacturing.

In addition, as can be seen in Fig. 7(a), according to the thermal cycle curve measured by K-type thermocouple and paperless thermometer (HIOKI LR8431), the thermal history of DLD single layer 12CrNi2 alloy steel experienced a rapid solidification process in the first few
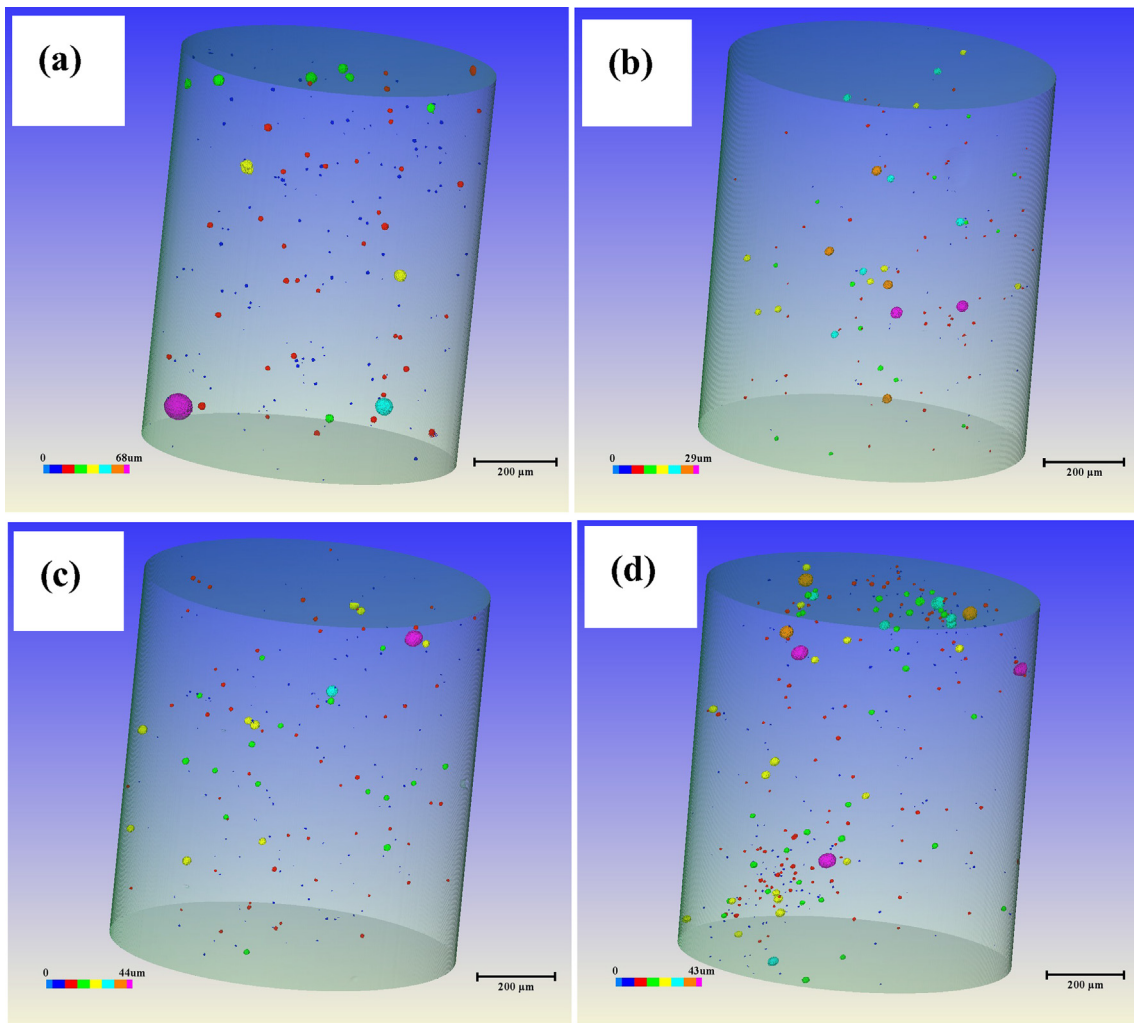
Table 1
Process parameters.

Sample	P (W)	V (mm/s)	ΔZ (mm)	Ov (%)	R (g/min)
1	2000	4	0.7	35	7.5
2	2000	5	0.7	35	7.5
3	2000	6	0.7	35	7.5
4	2000	7	0.7	35	7.5

of the molten pool, inducing a contact between the surrounding molten pools. Once the connection was built, the gas generated by the reaction during the DLD process or the gas from external atmosphere was hard to remove and it finally formed a pore defect in the sample 1 [18,19]. Besides, high laser scanning speed (7 mm/s) could lead to a low energy input. Under this condition, the 12CrNi2 alloy steel powders might be incompletely melted due to the insufficient laser energy input, which increased the porosity of sample 4 [20]. In addition, sample 1 and sample 4 had larger average void's volume than sample 2 and sample 3. The largest void's volume in sample 4 was 158,568 μm^3, which had an adverse effect on the mechanical properties of DLD-processed 12CrNi2 samples, because it was more likely to be a favorable location for crack

Table 2
Experimental parameters of wear test.

Counterpart	Load (N)	Temperature (℃)	Wear time (min)	Wear velocity (mm/min)	Wear length (mm)
GCr15	10	25	40	150	7

Fig. 4. 3D void distributions of the samples fabricated at different laser scanning speed. (a) 4 mm/s, (b) 5 mm/s, (c) 6 mm/s, (d) 7 mm/s.

seconds and then a solid state phase transformation process. Due to the thermal accumulation effect, the temperature range of subsequent phase transformation was usually remained about 500–600 °C. According to simulated TTT curve of 12CrNi2 alloy steel in Fig. 7(b), it can be predicted that the main phase of DLD-processed 12CrNi2 alloy steel was banite. At the same time, different laser scanning speed resulted in different cooling rates, so the amount of bainite, ferrite and martensite would vary with the laser scanning speed.

The optical micrograph of 12CrNi2 alloy steel sample fabricated by DLD is shown in Fig. 8(a). It can be seen that the microstructure of DLD-processed sample was fine due to the extremely fast cooling rate, which exerted positive influence on the comprehensive performance of the
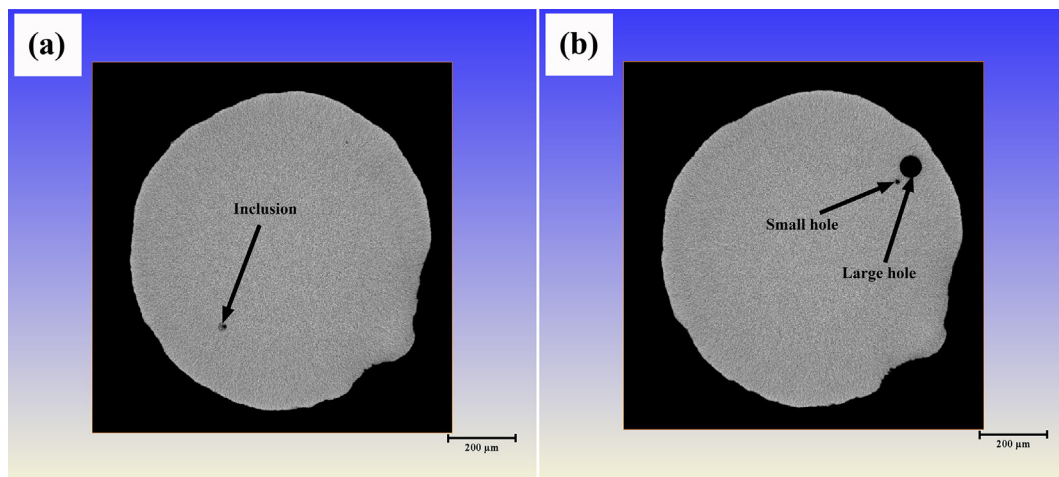

Fig. 5. Different types of defect topography in the DLD-processed samples: (a) Inclusion, (b) Pores.

Table 3
Defect data analysis of DLD-processed 12CrNi2 samples.

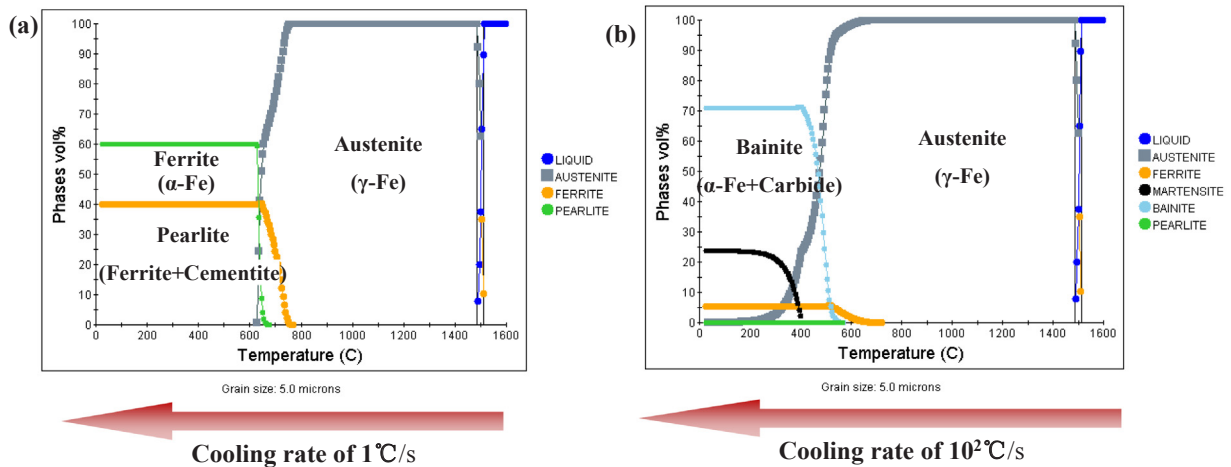| Data	Sample 1	Sample 2	Sample 3	Sample 4
Total scanned volume (μm^3)	454,325,888	531,219,072	611,816,512	556,845,888
Total detected defect volume (μm^3)	342,908	96,220	157,397	412,240
Average void's volume (μm^3)	1723	718	799	1168
Largest void's volume (μm^3)	158,568	11,959	42,633	40,963

Fig. 6. (a) Equilibrium phase diagram of 12CrNi2 alloy steel, (b) Non-equilibrium phase diagram of 12CrNi2 alloy steel.

final part. Besides, the main phase observed in as-deposited sample was bainite including lath bainite (LB) and granular bainite (GB), which was consistent with the above simulation results via JMATPRO software.

Fig. 8(b) demonstrates the XRD spectra of DLD-processed 12CrNi2 alloy steel samples. The phase of α-Fe (M), where M represented alloy elements (e.g. Cr, Mn), and a small amount of $Cr_{23}C_6$ were clearly observed in the XRD pattern. Because the laser scanning speed of different samples fluctuated in a small range, indicating that the various phases were formed under the approximately same thermodynamic conditions. Hence, there was no significant difference in the XRD peaks among the tested samples [23,24]. It is known that bainite, martensite and ferrite are all body-centered cubic (BCC) structures, and therefore they could not be distinguished by diffraction peaks. Granular bainite consists of bainite ferrite and carbon-rich island structures, so $Cr_{23}C_6$ detected in the as-deposited sample was a kind of carbon-rich island structures in GB. In addition, compared to the standard 2θ locations of α-Fe and $Cr_{23}C_6$, all diffraction peaks in Fig. 8(b) shifted a little bit to higher

Bragg angles because Fe and other alloy elements could form solid solution, leading to lattice distortion. Moreover, the stress produced by rapid heating and cooling process could also result in the shift of 2θ location.

3.3. The analysis of microstructural evolution

Fig. 9 shows the SEM morphology of the as-deposited samples prepared at different laser scanning speed. As the laser scanning speed increased from 4 mm/s to 7 mm/s, the cooling rate of the material increased gradually, leading to refined microstructure. As shown in Fig. 9(a), when the laser scanning rate was 4 mm/s, the main phase of DLD-processed sample was granular bainite (GB) and massive ferrite. The reason for the occurrence of massive ferrite was transformation temperature of ferrite was higher than that of bainite, so more massive ferrite formed as decreasing the cooling rate. As shown Fig. 9(b), massive ferrite disappeared gradually, while a small amount of lath
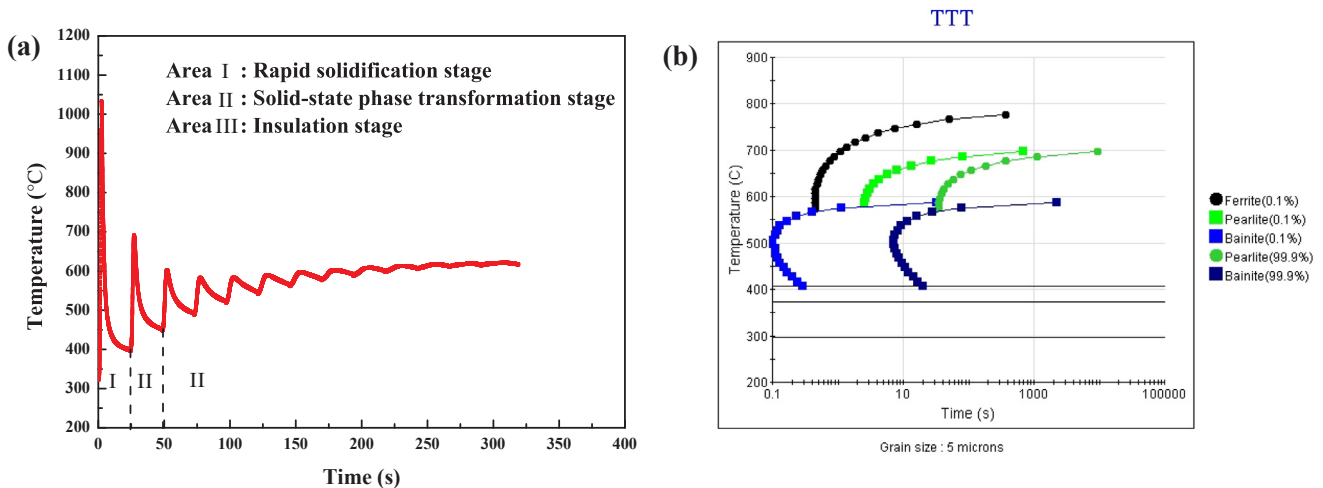

Fig. 7. (a) Thermal cycle curve of DLD single layer 12CrNi2 alloy steel, (b) Simulated TTT curve of 12CrNi2 alloy steel.
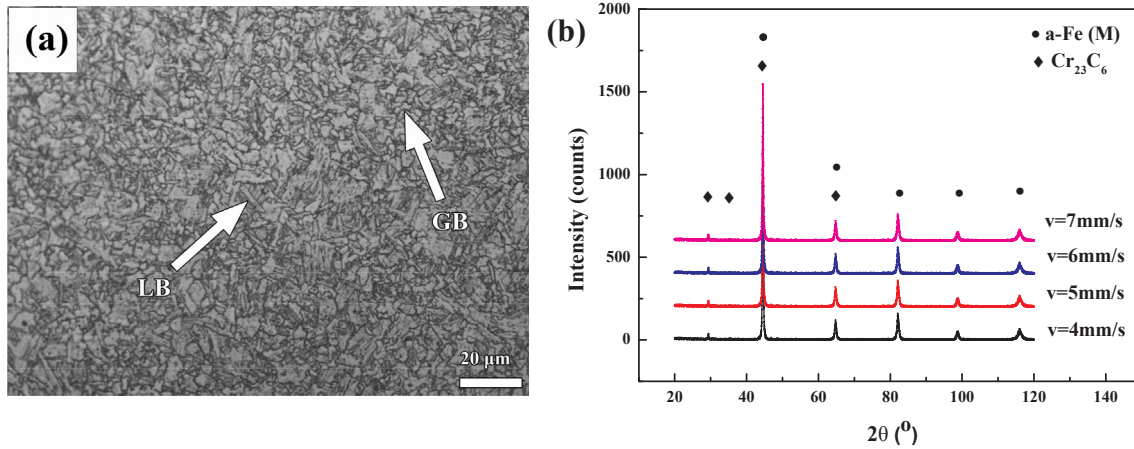
Fig. 8. (a) Metallographic image of as-deposited 12CrNi2 sample, (b) XRD spectra of as-deposited 12CrNi2 sample.

bainite (LB) appeared in the sample fabricated at laser scanning speed of 5 mm/s. From Fig. 9(c)–(d), when the laser scanning speed reached 6–7 mm/s, a small amount of martensite appeared in the DLD-processed 12CrNi2 alloy steel samples, and the amount of LB showed an upward trend with the increase of laser scanning speed.

In order to quantitatively analyze the change of the phase content with the laser scanning speed, this study used image processing software to calculate the fractions of different phases in four as-deposited samples [25,26], as shown in Fig. 10. It can be seen that when the laser scanning speed was 4 mm/s, the proportion of ferrite was 55.6% and that of GB was 40.8%, while that of martensite was almost zero. As laser scanning speed further increased, ferrite transformed into granular bainite. When the laser scanning speed reached 6 mm/s, the percentage of granular bainite was about 72.2%, which was about 77% higher than that in the sample fabricated at laser scanning speed of 4 mm/s. As the laser scanning speed increased to 7 mm/s, part of GB transformed into the LB, and therefore the proportion of LB rise to 29.9%. Meanwhile,

4.9% martensite appeared in sample 4 due to the fast cooling rate.

To establish the relationship between the percentage of different phases and the laser scanning speed, the contents of different phases at 4 mm/s, 4.5 mm/s, 5 mm/s, 5.5 mm/s, 6 mm/s, 6.5 mm/s and 7 mm/s were calculated. The relationship between the percentage of different phases and laser scanning speed was fitted, as shown in Fig. 11. In addition, the fitting functions are shown in Eqs. (2)–(5), as follows:

$$z_1 = -3.63x^3 + 70.42x^2 - 488.84x + 954.47 \tag{2}$$

$$z_2 = -15.12x^2 + 170.1x - 396.44 \tag{3}$$

$$z_3 = 0.65x^3 - 6.89x^2 + 20.9x - 8.16 \tag{4}$$

$$z_4 = 3.07x^3 - 31.22x + 77.7 \tag{5}$$

where x is laser scanning speed, mm/s; z_1, z_2, z_3, and z_4 represent the percentage of ferrite, granular bainite, lath bainite, and martensite, respectively, %. From Fig. 11(a), the percentage of ferrite exhibited fluctuating status. As shown in Fig. 11(b), with the change of laser
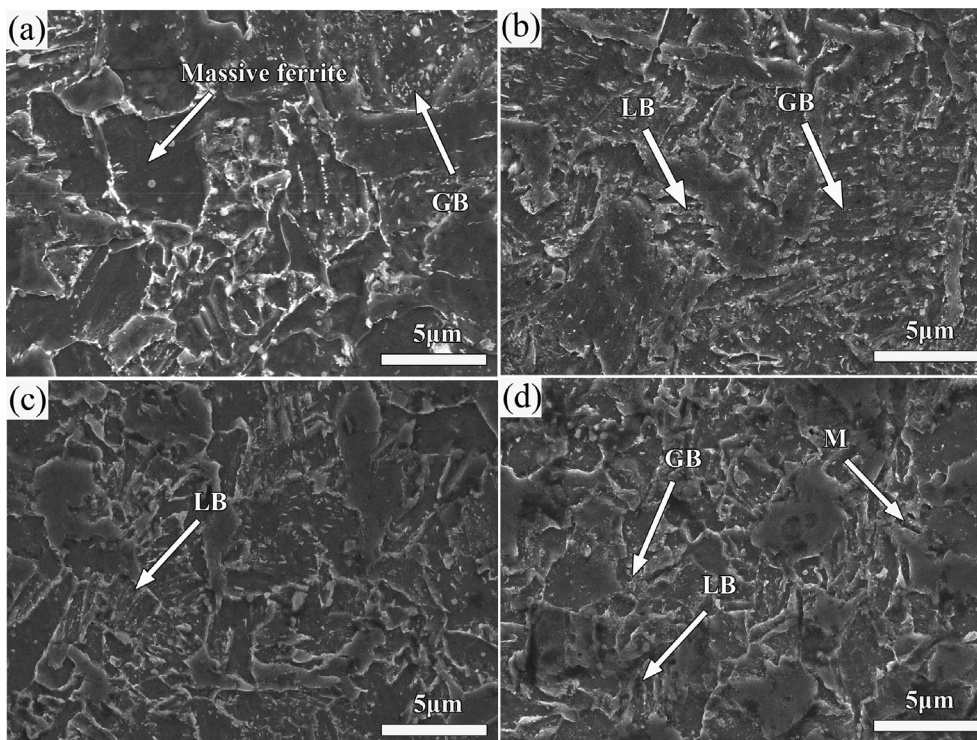

Fig. 9. Typical SEM images of different samples: (a) sample 1, (b) sample 2, (c) sample 3, (d) sample 4.
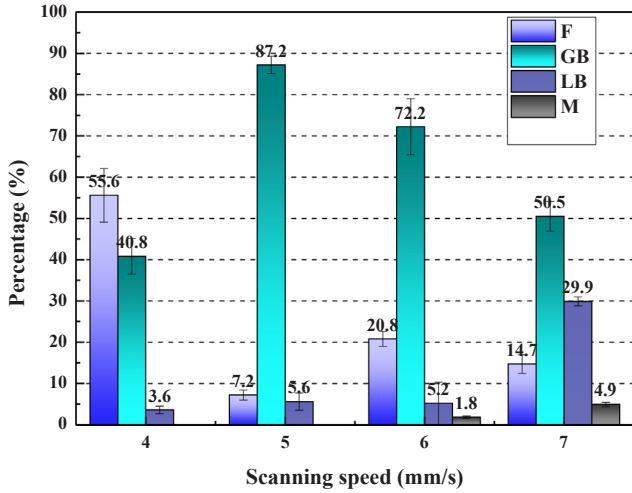
Fig. 10. Percentage of different phases in four as-deposited samples.

scanning speed, the proportion of GB showed a quadratic function. Moreover, it can be calculated that the percentage of GB reached a maximum of 81.8% when the laser scanning speed was 5.6 mm/s. Fig. 11(c) demonstrates the proportion of LB had a clear upward trend after 6 mm/s. As shown in Fig. 11(d), the proportion of martensite exhibits a similar tendency to LB at different laser scanning speeds, and the phase content thereof increases when the scanning speed exceeds 6 mm/s.

Only four kinds of phases were contained in the DLD-processed 12CrNi2 alloy steel sample, as shown in Eq. (6):

$$z_1 + z_2 + z_3 + z_4 = 100 \tag{6}$$

Therefore, the total fitting expression of the effect of laser scanning speed on the microstructure of DLD-processed 12CrNi2 alloy steel could be obtained, as follows:

$$z = -2.98x^3 + 52.48x^2 - 140.96x - 180.27 \tag{7}$$

As shown in Fig. 12, the central portion of DLD-processed 12CrNi2 alloy steel samples exhibited anisotropy, because the reciprocating scanning path would cause repeated changes in heat flow direction. In addition, the effect of laser scanning speed on the grain size of deposited sample is clearly shown in Fig. 12. With the laser scanning speed increasing, the grain size was significantly refined. The grain sizes of the four as-deposited samples were counted in the range of $1-20\ \mu m^2$ to be $5.89\ \mu m^2$, $5.11\ \mu m^2$, $4.90\ \mu m^2$, and $3.44\ \mu m^2$, respectively. Since bainite was the main phase of DLD-processed alloy steel samples, according to the bainite formation kinetics theory proposed by Ravi et al. [27,28], the nucleation driving force ΔG of bainite can be expressed by formula (8) :

$$\Delta G = T_h - T \tag{8}$$

where T is the transformation temperature of bainite; T_h is the temperature at $\Delta G_m = G_N$, G_N is a general nucleation function, ΔG_m is the maximum driving force of nucleation, as shown by Eq. (9):

$$\Delta G_m = G_m^{\alpha} - G_m^{\gamma} \tag{9}$$

where G_m^{α} and G_m^{γ} are bainitic ferrite free energy and austenite free energy, respectively. When the laser scanning speed was increased from 4 mm/s to 7 mm/s, the cooling rate showed an upward trend, and the bainite transformation temperature T gradually decreased. According to Eq. (8), the bainite nucleation driving force increased as laser
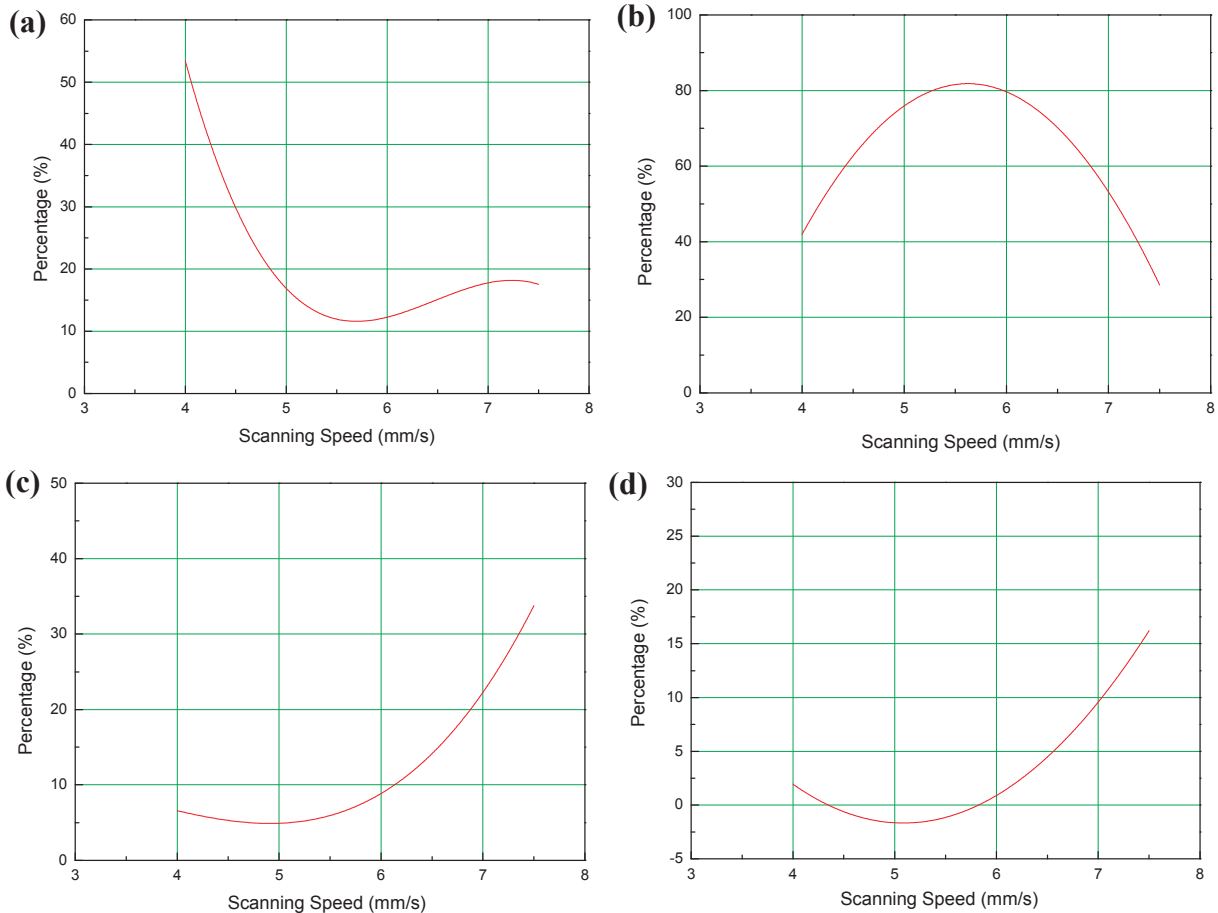

Fig. 11. Fitting curves of different phase percentage: (a) F, (b) GB, (c) LB, (d) M.
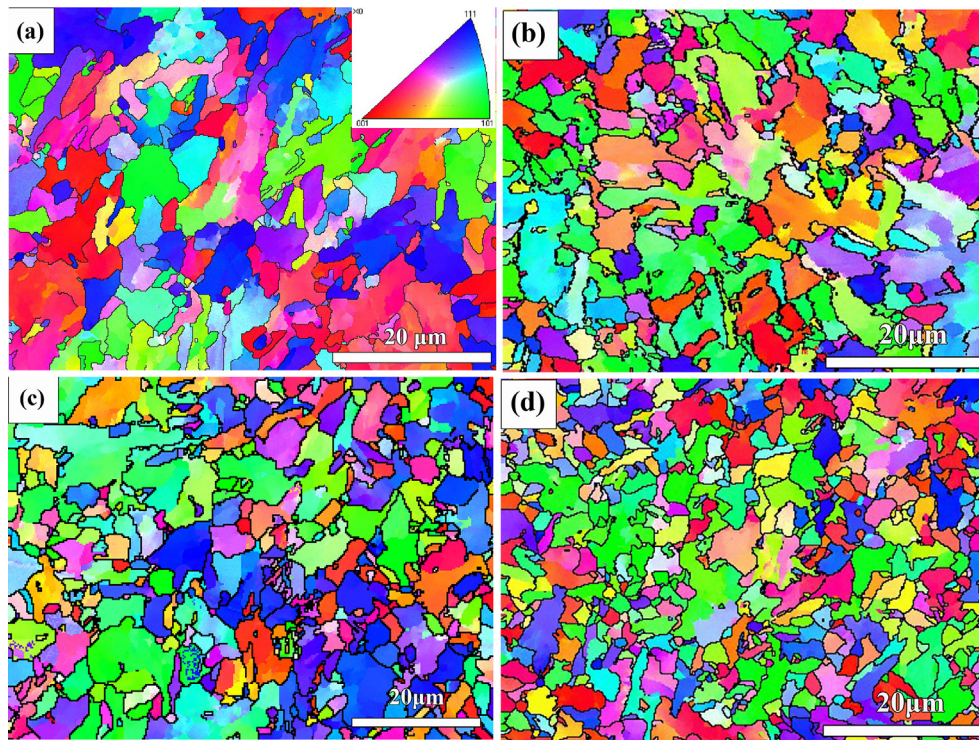
Fig. 12. IPF figures of DLD-processed 12CrNi2 samples: (a) sample 1, (b) sample 2, (c) sample 3, (d) sample 4.

scanning speed increasing, indicating the grain size becoming smaller. Compared to our previous work, the effect of laser scanning speed on the grain size of as-deposited alloy steel samples was greater than that of laser power.

With the increase of laser scanning speed, the FCC phase contents in the four samples were 0.255%, 0.028%, 0.404%, and 0.606%, respectively. It can be seen that the amount of austenite in the DLD-processed samples was extremely small. One reason was austenite was too fine to be accurately detected with the scanning step of 0.2. The more important reason was that during the equilibrium transformation of Fe-Cr-Ni alloy, the sample solidified into primary δ-ferrite at first, followed by complete austenite transformation, and then bainite and martensite occurred with further cooling. However, DLD 12CrNi2 alloy steel was a rapid cooling process, according to the simulated results by thermo-dynamic software, the austenite transformation temperature of 12CrNi2 alloy steel was 838 ℃ and the bainite transformation temperature was 589 ℃ when the cooling rate was 10^2 ℃/s, so FCC phase transformation usually occurred in the temperature range of 589–838 ℃. As shown in Fig. 7(a), the duration of this transformation stage was ~1.5 s. Therefore, during the DLD 12CrNi2 alloy steel process, since the transformation of δ-ferrite → γ-austenite did not have enough time and driving force, δ-ferrite rapidly passed through the stable temperature range of austenite without being converted into the FCC phase until reaching the stable transformation range of bainite or martensite [29].

In addition, as shown in Fig. 13, the effect of laser scanning speed on the grain size of as-deposited samples was fitted, and the fitting equation is as follows:

$$z_5 = -0.3033x^3 + 4.835x^2 - 25.79x + 51.11 \qquad (10)$$

It can be seen that within a suitable laser scanning speed range, the grain size decreased as increasing the laser scanning speed. Moreover, the grain size of the sample had a low rate of change from 4 mm/s to 6 mm/s, and the average rate of change was 0.5 $\mu m^2/mm \cdot s^{-1}$, while the average rate of change was 1.5 $\mu m^2/mm \cdot s^{-1}$ when the range of laser scanning speed was from 6 mm/s to 7 mm/s. Therefore, it can be inferred that fine control should be performed in the range of 6 mm/s to 7 mm/s when controlling the laser scanning rate.
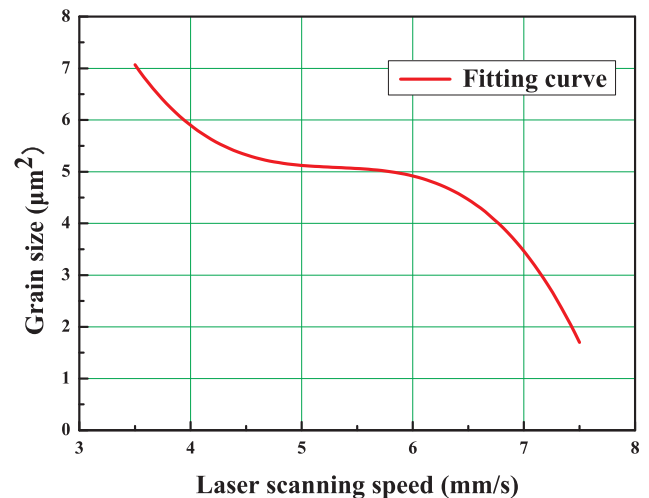

Fig. 13. Fitting curve of the grain size of four as-deposited samples fabricated at different laser scanning speed.

Fig. 14 illustrates TEM micrographs of DLD-processed 12CrNi2 alloy steel samples. By observing the SEM morphology of the samples prepared at different laser scanning speed, it can be found that the amount of martensite was extremely small, so it was difficult to find clear lath martensite under TEM. As shown in Fig. 14(a) and (b), it was a mixed microstructure of granular bainite (GB) and polygonal ferrite (PF). Compared with PF, there was a large amount of carbon-rich island structures in GB, which distributed dispersedly in the grains. The size of island structure in GB was too small to measure the diffraction spot, but according to the results of XRD analysis, it is presumed that the island structure in GB was mainly $Cr_{23}C_6$ carbide. In addition, it can be found that $Cr_{23}C_6$ precipitated not only in the grains (marked by the red circle in Fig. 14(a) and (b)), but also on the grain boundaries (marked by the blue circle in Fig. 13(a) and (b)) [30]. Fig. 14(c) shows the TEM micrograph of LB, and LB had relatively twisted boundaries. Moreover,
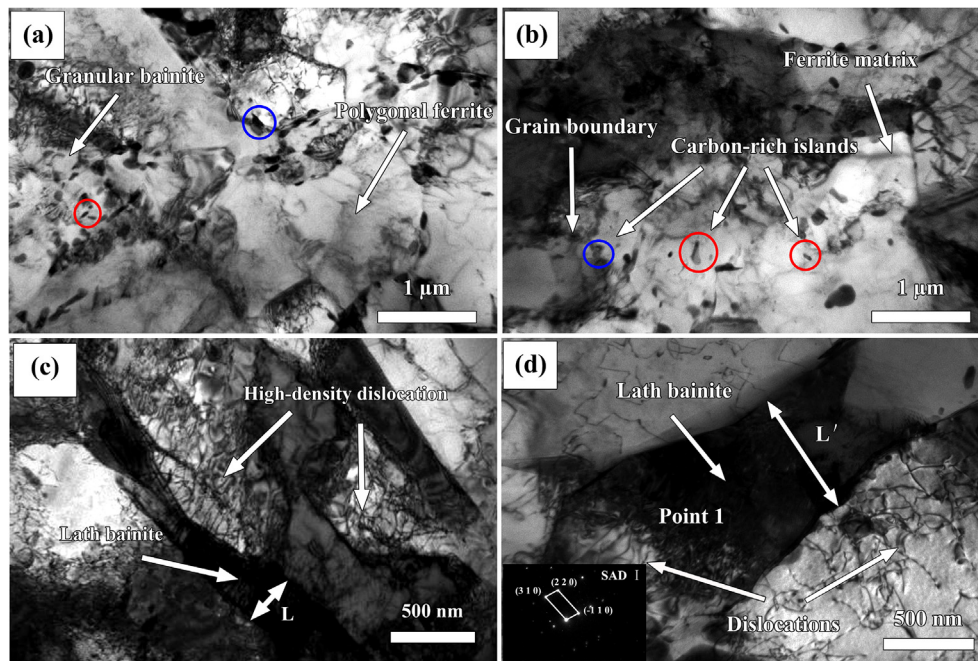
Fig. 14. TEM micrographs of DLD-processed 12CrNi2 alloy steel samples.

the width of bainite ferrite lath L reached 300–400 nm. During the rapid melting and solidification process, Much heat stress was introduced into the 12CrNi2 alloy steel samples due to differences in coefficient of thermal expansion (CTE) of component phases, which efficiently suppressed the phase transformation of fabricated samples, resulting in a high dislocation density [31–33]. As can be seen in Fig. 14(d), there were some bainite lath with the width L' of 500–600 nm could be observed in as-deposited samples. The reason for this phenomenon was that direct laser deposition 12CrNi2 alloy steel was a high-energy input process, and thus LB generated in DLD process was wider and more distorted than the medium or low energy input process due to lower cooling rate [34].

3.4. Microhardness

Fig. 15 demonstrates the Vickers microhardness of the samples fabricated at different laser scanning speed. From Fig. 15, the microhardness curves of samples showed varying degrees of fluctuation. The upmost layers of the all samples possessed high hardness values. Below
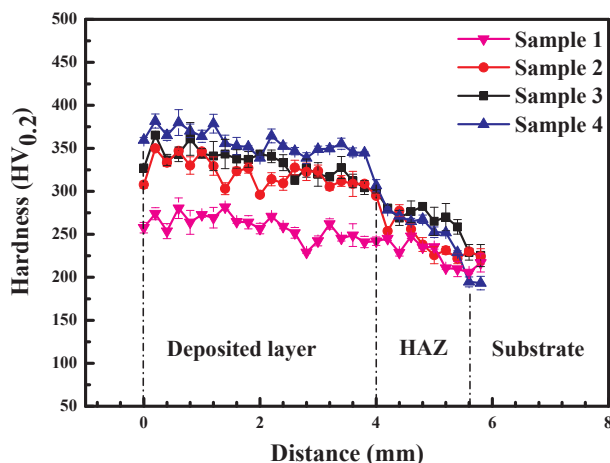

Fig. 15. Microhardness profile along the cross section of four as-deposited samples.

the top layers, the tempering factors produced by high energy laser beam resulted in the variations of the hardness values along the build direction. Due to the heterogeneous microstructure and micro-defects, the microhardness of all DLD-processed 12CrNi2 alloy steel samples showed high variance [35]. Due to the low content of carbides, the comprehensive properties of prepared specimens, including the average hardness, depend on the amount of ferrite, GB, and LB. In general, compared to ferrite, bainite had higher microhardness, and the microhardness of LB was higher than that of GB [15]. The average microhardness of the samples fabricated at different laser scanning speed from 4 mm/s to 7 mm/s was 259 ± 6, 320 ± 6, 332 ± 8 and 355 ± 6 $HV_{0.2}$, respectively, and it was an obvious regularity that the microhardness of the sample increased with the increase of laser scanning speed. One reason of this phenomenon was with increasing the laser scanning speed, the microstructure transformed from ferrite into GB, followed by transforming into LB. The other reason was according to EBSD analysis, the grain size of four samples showed a downward trend with increasing the laser scanning speed, and fine grains always meant better microhardness.

As shown in Fig. 16, different as-deposit region of the sample 4 exhibited various phases, leading to different microhardness. From Fig. 16(a), compared to the other portions of the as-deposited layer, the top portion of the sample had the highest microhardness of 341 $HV_{0.2}$, because heat conduction and convective heat transfer between the top portion and external atmosphere would result in more rapid cooling rate, leading to more martensite formed. As shown in Fig. 16(b), the main microstructure of the middle as-deposited was bainite, whose microhardness (312 $HV_{0.2}$) was lower than martensite. The HAZ (heat affected zone) exhibited lower microharness of 289 $HV_{0.2}$ than the as-deposited layer, as shown in Fig. 16(c).

3.5. Wear resistance

The mean friction coefficient of four DLD-processed 12CrNi2 alloy steel samples is 0.757, 0.291, 0.282, 0.528, respectively. It can be seen that the friction coefficient of sample 3 is the lowest, which indicates the sample 3 has the best wear resistance.

Fig. 17 shows the SEM micrographs and 3D surface of the worn tracks of four samples. The worn surface of sample 1 had numerous
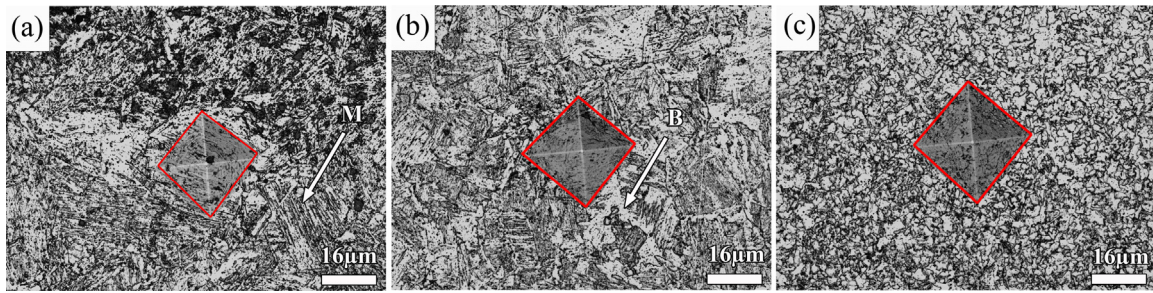
Fig. 16. Microhardness of different parts of DLD-processed 12CrNi2 alloy steel sample. (a) top, (b) middle, (c) HAZ.
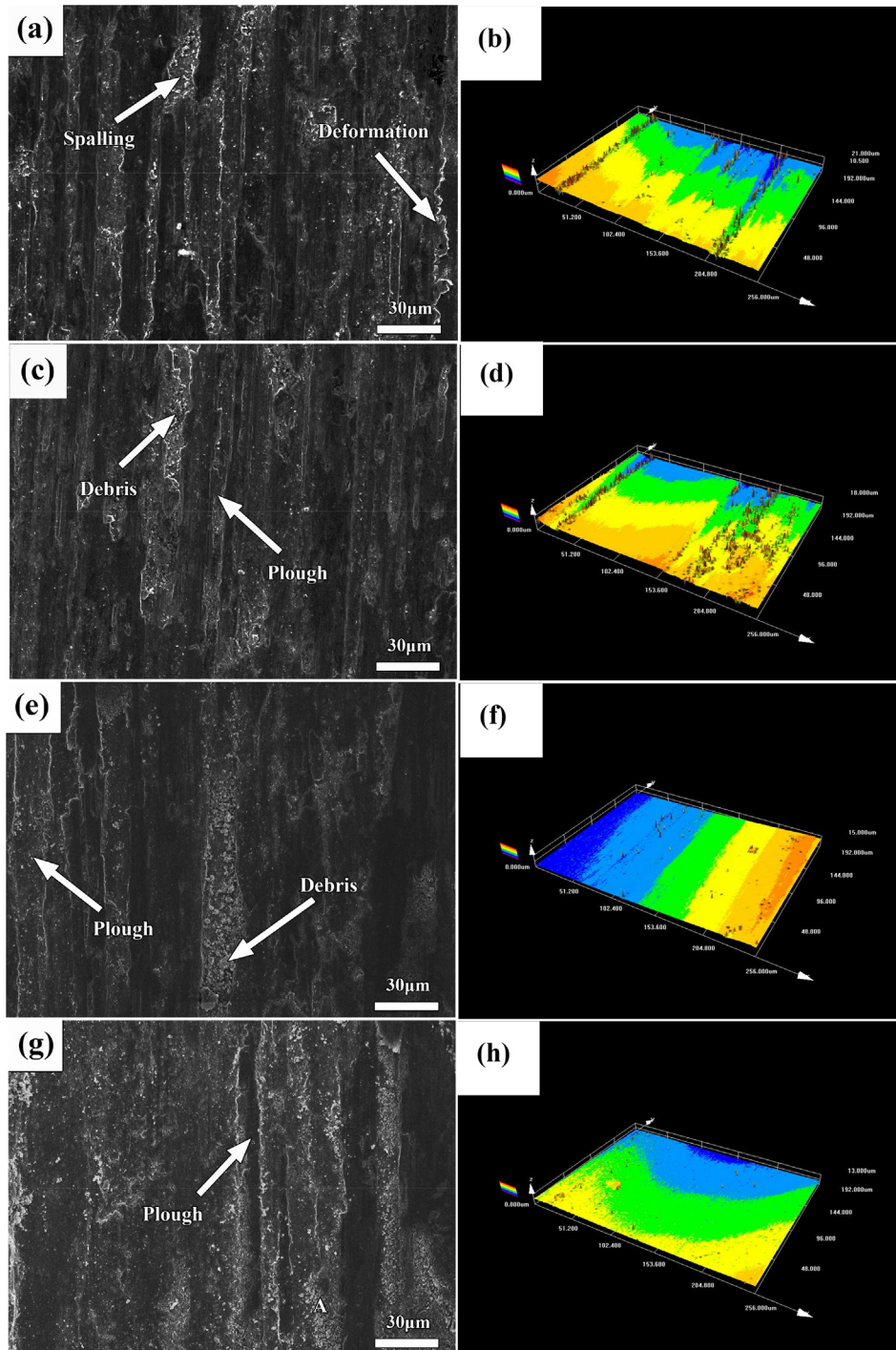

Fig. 17. Worn morphology and three-dimensional roughness of worn track of as-deposited samples: (a, b) 4 mm/s, (c, d) 5 mm/s, (e, f) 6 mm/s, (g, h) 7 mm/s.

spallings and plastic deformation, indicating that the microhardness of sample 1 was not enough to resist the normal and tangential force during the dry sliding wear test, as shown in Fig. 17(a). From Fig. 17(b), there are some adhesive patches and many ploughed furrows on the worn surface of sample 2, so abrasive wear was the main wear mechanism of sample 2. As can be seen in Fig. 17(c), the worn surface of sample 3 was much smoother than that of other samples, and it had some shallow ploughed furrows coupled with some debris, and therefore the wear mechanism of sample 3 was mainly abrasive wear. For sample 4, as shown in Fig. 17(g), the wt.% of oxygen at selected position (Point A) reached 20.49, because the surface of sample 4 could generated a large amount of heat and then oxidized when the wear test was conducted in air [36,37]. Hence, the wear mechanism of sample 4 was mainly oxidative wear.

In addition, this study used confocal laser scanning microscopy (OSL3000) to characterize the three-dimensional surface of the worn track, as shown in Fig. 17(b), (d), (f) and (h). The average roughness of the worn tracks of four as-deposited samples was 0.21, 0.17, 0.09, and 0.12, respectively. As shown in Fig. 17(b), the roughness of the two long strips was higher than other locations of the worn surface, and it is speculated that two long strips were plough on the worn surface. From Fig. 17(d), the right area of the worn surface had higher roughness, which displayed irregular in shape, and according to SEM morphology, this area might be debris or spalling. Fig. 17(f) and (h) showed smoother wear surface morphology, which also indicated that the wear resistance of sample 3 and 4 were better.

The results showed that sample 3 had the best wear resistance among the tested samples. High wear resistance not only required a high microhardness but also a suitable toughness. The island structures in the granular bainite were transformed from carbon-rich austenite regions, and thus a small amount of retained austenite in the granular bainite could improve the toughness of alloy steel samples. In addition, the dispersed island structures were distributed well in the matrix, and they interacted with the dislocations to increase the strength of alloy steel. As can be seen in Fig. 15, sample 3 has the second-highest hardness of $332 \pm 8 \ HV_{0.2}$ and a large amount of island structures, and therefore sample 3 has better combination of strength and toughness than other samples to resist the force generated by the wear test [38,39].

3.6. Impact toughness

Impact toughness is one of the important indicators to measure the performance of DLD-processed 12CrNi2 alloy steel samples. The impact toughness a_{ku} (J/cm^2) was calculated by Eq. (11):

$$a_{ku} = A_{ku}/S \qquad (11)$$

where S is bottom notch cross-sectional area of the impact specimen, S = 0.8 cm^2; A_{ku} is the impact absorbed energy, J. A_{ku} and a_{ku} of four as-deposited samples fabricated at different laser scanning speed are listed in Table 4, and samples 1 and sample 2 exhibited the best impact toughness of a_{ku} = 80 J/cm^2. Wang [40] et al. researched that the impact toughness of 30CrMnSiA alloy parts fabricated by forged annealing and selective laser melting (SLM) reached 49.4 J/cm^2 and 14.3 J/cm^2, respectively, and it can be seen the impact toughness of

Table 4
Impact toughness of DLD-processed 12CrNi2 alloy steel.

Sample	A_{ku} (J)	a_{ku} (J/cm^2)	Reference
1	64.0	80.0	–
2	64.0	80.0	–
3	58.0	72.5	–
4	55.0	68.8	–
SLM-manufactured 30CrMnSiA alloy	11.4	14.3	[29]
FAed 30CrMnSiA alloy	39.5	49.4	[29]

DLD-manufactured 12CrNi2 alloy steel was better than SLM-manufactured and FAed 30CrMnSiA alloy steel.

Theoretically, the impact toughness of ferrite should be optimal, followed by granular bainite, and finally lath bainite, and thus it can be inferred that the impact toughness of DLD-processed 12CrNi2 alloy steel sample declined with changing the laser scanning speed from 4 mm/s to 7 mm/s. However, as can be seen in Table 4, the impact toughness of sample 1 was same as that of sample 2, because the room-temperature impact toughness was very sensitive to the internal defects of the DLD-processed sample. Based on the porosity analysis above, the porosity of sample 1 was lower than sample 2, leading to the same impact toughness value of them.

Fig. 18 showed the fracture surfaces of as-deposited 12CrNi2 samples. As shown in Fig. 18(a), the fracture surface of sample 1 consisted of plenty of uniform dimple structures, which meant a clear ductile fracture. The depth of dimples was usually considered as a measurement criteria of the ductility [41], and it was obvious the dimples in samples 1 were the deepest among four samples, indicating the optimal impact toughness. From Fig. 18(b), a large amount of fine dimples and some microvoids occurred on the fracture surface of sample 2, so the fracture mechanism of sample 2 was micro-porous aggregation fracture. In addition to plenty of dimples and several tear ridges, some unmelted particles, a kind of process-induced defect, could be seen in Fig. 18(c). As can be seen in Fig. 18(d), there was some tear ridges observed on the fracture surface. In addition, some smoother and flatter cleavage planes could be seen in Fig. 17(d), indicating faster crack propagation. The morphology of fracture surface in Fig. 17(d) coincided with the lowest impact toughness of sample 4 (a_{ku} = 68.8 J/cm^2).

4. Conclusion

The microstructural evolution and performance of DLD 12CrNi2 alloy steel under different laser scanning speed has been studied in this paper. The main conclusions are listed as follows:

(1) As laser scanning speed increased, the proportion of ferrite decreased from 55.6% to 14.7%, while that of martensite increased from 0% to 14.9%. In addition, when there was an increase in laser scanning speed, granular bainite (GB) transformed into lath bainite (LB). When laser scanning speed was 7 mm/s, the proportion of LB reached a maximum of 29.9%.

(2) The EBSD pattern of the as-deposited sample showed anisotropy due to the complex heat flux direction during DLD 12CrNi2 alloy steel. In addition, as the laser scanning speed increased, the transformation temperature of bainite T decreased gradually, and the nucleation driving force of bainite ΔG increased, and thus the grain size showed a significant downward trend, from 5.89 μm^2 to 3.44 μm^2.

(3) According to the change of phase content and grain size at different laser scanning speed, the total fitting expression of the relationship between laser scanning speed and different phase fractions was $z = -2.98x^3 + 52.48x^2 - 140.96x - 180.27$, and the fitting equation between laser scanning speed and grain size was $z_5 = -0.3033x^3 + 4.835x^2 - 25.79x + 51.11$.

(4) The DLD-processed 12CrNi2 alloy steel sample fabricated at 7 mm/s had the optimal microhardness of $355 \pm 6 \ HV_{0.2}$. Moreover, the as-deposited sample fabricated at 6 mm/s exhibited the best wear resistance, the coefficient of friction was 0.282. The sample fabricated at 4 mm/s had the best impact toughness of a_{ku} = 80.0 J/cm^2 due to the large amount of ferrite phase.

Declaration of Competing Interest

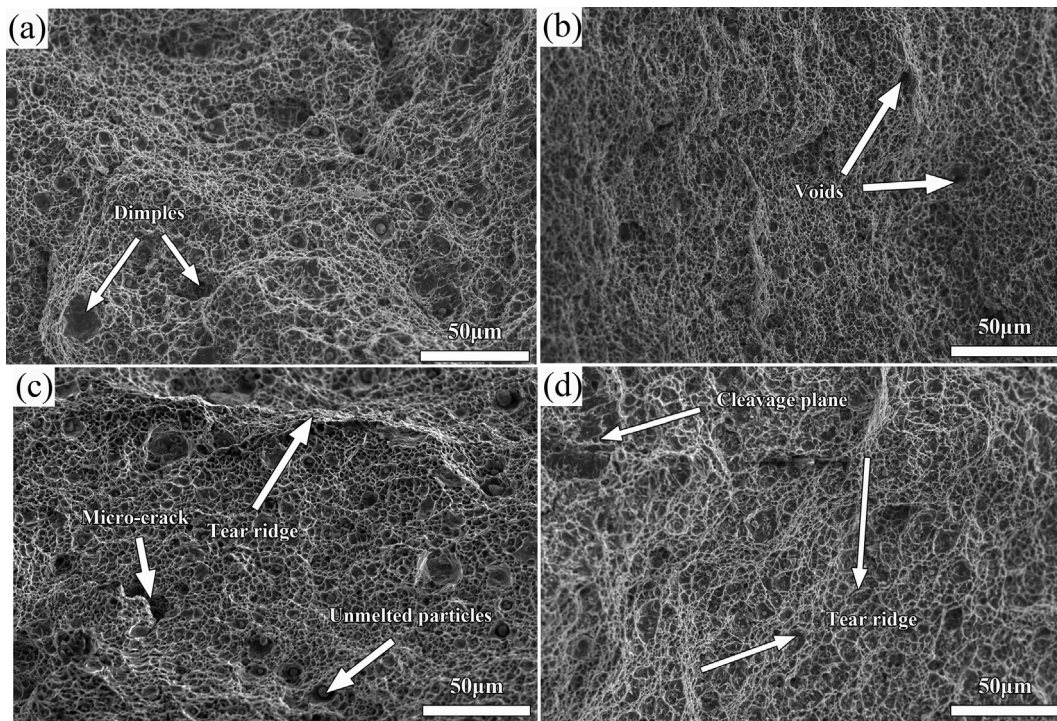The authors declared that there is no conflict of interest.

Fig. 18. The SEM images of impact fracture surfaces: (a) sample 1, (b) sample 2, (c) sample 3, (d) sample 4.

Acknowledgements

Data availability statement

The raw/processed data required to reproduce these findings cannot be shared at this time as the data also forms part of an ongoing study.

Appendix A. Supplementary material

Supplementary data to this article can be found online at https://doi.org/10.1016/j.optlastec.2019.106041.

References

[1] J.J.S. Dilip, G.D.J. Ram, T.L. Starr, B. Stucker, Selective laser melting of HY100 steel: process parameters, microstructure and mechanical properties, Addit. Manuf. 13 (2017) 49–60.

[2] F. Caiazzo, Laser-aided Directed Metal Deposition of Ni-based superalloy powder, Opt. Laser Technol. 103 (2018) 193–198.

[3] T. DebRoy, H.L. Wei, J.S. Zuback, T. Mukherjee, J.W. Elmer, J.O. Milewski, et al., Additive manufacturing of metallic components-process, structure and properties, Prog. Mater Sci. 92 (2018) 112–224.

[4] S.M. Thompson, L. Bian, N. Shamsaei, A. Yadollahi, An overview of Direct Laser Deposition for additive manufacturing; Part I: Transport phenomena, modeling and diagnostics, Addit. Manuf. 8 (2015) 36–62.

[5] T.T. Guan, S.Y. Chen, X.T. Chen, J. Liang, C.S. Liu, M. Wang, Effect of laser incident energy on microstructures and mechanical properties of 12CrNi2Y alloy steel by direct laser deposition, J. Mater. Sci. Technol. 35 (2019) 395–402.

[6] N. Shamsaei, A. Yadollahi, L. Bian, S.M. Thompson, An overview of Direct Laser Deposition for additive manufacturing; Part II: Mechanical behavior, process parameter optimization and control, Addit. Manuf. 8 (2015) 12–35.

[7] P. Guo, B. Zou, C.Z. Huang, H.B. Gao, Study on microstructure, mechanical properties and machinability of efficiently additive manufactured AISI 316L stainless steel by high-power direct laser deposition, J. Mater. Process. Technol. 240 (2017) 12–22.

[8] M.W. Wei, S.Y. Chen, L.Y. Xi, J. Liang, C.S. Liu, Selective laser melting of 24CrNiMo steel for brake disc: fabrication efficiency, microstructure evolution, and properties, Opt. Laser Technol. 107 (2018) 99–109.

[9] J.X. Fang, S.Y. Dong, Y.J. Wang, B.S. Xu, Z.H. Zhang, D. Xia, W.B. Ren, P. He, Microstructure and properties of an as-deposited and heat treated martensitic stainless steel fabricated by direct laser deposition, J. Manuf. Process. 25 (2017) 402–410, https://doi.org/10.1016/j.jmapro.2016.12.014.

[10] G. Casalino, S.L. Campanelli, N. Contuzzi, A.D. Ludovico, Experimental investigation and statistical optimisation of the selective laser melting process of a maraging steel, Opt. Laser Technol. 65 (2015) 151–158.

[11] X.L. Wang, D.W. Deng, H.L. Yi, H.Y. Xu, S.H. Yang, H.C. Zhang, Influences of pulse laser parameters on properties of AISI316L stainless steel thin-walled part by laser material deposition, Opt. Laser Technol. 92 (2017) 5–14.

[12] T. Kurzynowski, K. Gruber, W. Stopyra, B. Kuźnicka, E. Chlebus, Correlation between process parameters, microstructure and properties of 316 L stainless steel processed by selective laser melting, Mater. Sci. Eng., A 718 (2018) 64–73.

[13] B. Chen, J. Mazumder, Role of process parameters during additive manufacturing by direct metal deposition of Inconel 718, Rapid Prototyping J. 1 (2017).

[14] K. Zhang, S.J. Wang, W.J. Liu, X.F. Shang, Characterization of stainless steel parts by Laser Metal Deposition Shaping, Mater. Des. 55 (2014) 104–119.

[15] Y. Zhou, S.Y. Chen, X.T. Chen, T. Cui, J. Liang, C.S. Liu, The evolution of bainite and mechanical properties of direct laser deposition 12CrNi2 alloy steel at different laser power, Mater. Sci. Eng., A 742 (2019) 150–161.

[16] L. Cao, S.Y. Chen, M.W. Wei, Q. Guo, J. Liang, C.S. Liu, M. Wang, Effect of laser energy density on defects behavior of direct laser depositing 24CrNiMo alloy steel, Opt. Laser Technol. 111 (2019) 541–553.

[17] A. Yadollahi, N. Shamsaei, S.M. Thompson, A. Elwany, L. Bian, Effects of building orientation and heat treatment on fatigue behavior of selective laser melted 17–4 PH stainless steel, Int. J. Fatigue 94 (2017) 218–235.

[18] H.J. Gong, R. Khalid, H.F. Gu, T. Starr, B. Stucker, Analysis of defect generation in Ti-6Al-4V parts made using powder bed fusion additive manufacturing processes, Addit. Manuf. 1–4 (2014) 87–98.

[19] G.W. Wang, J.J. Liang, Y.H. Yang, Y. Shi, Y.Z. Zhou, T. Jin, X.F. Sun, Effects of scanning speed on microstructure in laser surface-melted single crystal superalloy and theoretical analysis, J. Mater. Sci. Technol. 34 (2018) 1315–1324.

[20] C. Liu, M. Zhang, C.J. Chen, Effect of laser processing parameters on porosity, microstructure and mechanical properties of porous Mg-Ca alloys produced by laser additive manufacturing, Mater. Sci. Eng., A 703 (2017) 359–371.

[21] J.Y. Shao, G. Yu, X.L. He, S.X. Li, R. Chen, Y. Zhao, Grain size evolution under different cooling rate in laser additive manufacturing of superalloy, Opt. Laser Technol. 119 (2019) 105662.

[22] P.F. Zuo, S.Y. Chen, M.W. Wei, J. Liang, C.S. Liu, M. Wang, Thermal behavior and grain evolution of 24CrNiMoY alloy steel prepared by pre-laid laser cladding technology, Opt. Laser Technol. 119 (2019) 105613.

[23] X.Y. Jiao, J. Wang, C.M. Wang, Z.Q. Gong, X.X. Pang, S.M. Xiong, Effect of laser scanning speed on microstructure and wear properties of T15M cladding coating fabricated by laser cladding technology, Opt. Laser Eng. 110 (2018) 163–171.

[24] W. Li, J. Liu, Y. Zhou, S. Li, S.F. Wen, Q.S. Wei, C. Yan, Y.S. Shi, Effect of laser scanning speed on a Ti-45Al-2Cr-5Nb alloy processed by selective laser melting: Microstructure, phase and mechanical properties, J. Alloys Compd. 688 (2016) 626–636.

[25] ASTM E45-2013 Standard test methods for determining the inclusion content of steel.

[26] ASTM E1382-1997 Standard test methods for determining average grain size using semiautomatic and automatic image analysis.

[27] A.M. Ravi, J. Sietsma, M.J. Santofimia, Bainite formation kinetics in steels and the dynamic nature of the autocatalytic nucleation process, Scr. Mater. 140 (2017) 82–86.

[28] A.M. Ravi, J. Sietsma, M.J. Santofimia, Exploring bainite formation kinetics distinguishing grain-boundary and autocatalytic nucleation in high and low-Si steels, Acta Mater. 105 (2016) 155–164.

[29] M. Alnajjar, F. Christien, K. Wolski, C. Bosch, Evidence of austenite by-passing in a stainless steel obtained from laser melting additive manufacturing, Addit. Manuf. 25 (2019) 187–195.

[30] I.A. Segura, L.E. Murr, C.A. Terrazas, D. Bermudez, J. Mireles, V.S.V. Injeti, et al., Grain boundary and microstructure engineering of Inconel 690 cladding on stainless-steel 316L using electron-beam powder bed fusion additive manufacturing, J. Mater. Sci. Technol. 35 (2019) 351–367.

[31] S. Cheruvathur, E.A. Lass, C.E. Campbell, Additive manufacturing of 17–4 PH stainless steel: Post-processing heat treatment to achieve uniform reproducible microstructure, JOM 68 (2016) 930–942.

[32] G.F. Sun, R. Zhou, J.Z. Lu, J. Mazumder, Evaluation of defect density, microstructure, residual stress, elastic modulus, hardness and strength of laser-deposited AISI 4340 steel, Acta Mater. 84 (2015) 172–189.

[33] H.F. Liu, H.J. Su, Z.L. Shen, E.Y. Wang, D. Zhao, M. Guo, J. Zhang, L. Liu, H.Z. Fu, Direct formation of Al2O3/GdAlO3/ZrO2 ternary eutectic ceramics by selective laser melting: microstructure evolutions, J. Eur. Ceram. Soc. 38 (2018) 5144–5152.

[34] A. Lambert-Perlade, A.F. Gourgues, A. Pineau, Austenite to bainite phase transformation in the heat-affected zone of a high strength low alloy steel, Acta Mater. 52 (2004) 2337–2348.

[35] J. Krell, A. Röttger, K. Geenen, W. Theisen, General investigations on processing tool steel X40CrMoV5-1 with selective laser melting, J. Mater. Process Tech. 255 (2018) 679–688.

[36] Y.L. Yuan, Z.G. Li, Effects of rod carbide size, content, loading and sliding distance on the friction and wear behaviors of $(Cr, Fe)_7C_3$-reinforced α-Fe based composite coating produced via PTA welding process, Surf. Coat. Technol. 278 (2014) 9–22.

[37] V. Jankauskas, R. Kreivaitis, D. Milčius, A. Baltušnikas, Analysis of abrasive wear performance of arc welded hard layers, Wear 265 (2008) 1626–1632.

[38] X.L. Xing, X.M. Yuan, Y.F. Zhou, X.W. Qi, X. Lu, T.H. Xing, et al., Effect of bainite layer by LSMCIT on wear resistance of medium-carbon bainite steel at different temperatures, Surf. Coat. Technol. 325 (2017) 462–472.

[39] L.C. Chang, The rolling/sliding wear performance of high silicon carbide-free bainitic steels, Wear 258 (2005) 730–743.

[40] L.Z. Wang, J.J. Wu, X.F. Huang, X.F. Hong, SLM-manufactured 30CrMnSiA alloy: Mechanical properties and microstructural effects of designed heat treatment, Opt. Laser Technol. 107 (2018) 89–98.

[41] L.W. Tong, L.C. Niu, S. Jing, L.W. Ai, X.L. Zhao, Low temperature impact toughness of high strength structural steel, Thin-Walled Struct. 132 (2018) 410–420.